



The ~ 50 Myr Old TOI-942c is Likely on an Aligned, Coplanar Orbit and Losing Mass

Huan-Yu Teng (滕环宇)^{1,2} , Fei Dai (戴飞)^{3,4,5} , Andrew W. Howard⁵ , Howard Isaacson^{6,7} , Ryan A. Rubenzahl^{5,10} , Isabel Angelo⁸ , and Alex S. Polanski⁹

¹ CAS Key Laboratory of Optical Astronomy, National Astronomical Observatories, Chinese Academy of Sciences, Beijing 100101, People's Republic of China; hyteng@bao.ac.cn

² Korea Astronomy and Space Science Institute, 776 Daedeok-daero, Yuseong-gu, Daejeon 34055, Republic of Korea

³ Institute for Astronomy, University of Hawai'i, 2680 Woodlawn Drive, Honolulu, HI 96822, USA

⁴ Division of Geological and Planetary Sciences, 1200 E California Boulevard, Pasadena, CA 91125, USA

⁵ Department of Astronomy, California Institute of Technology, Pasadena, CA 91125, USA

⁶ Department of Astronomy, University of California Berkeley, Berkeley, CA 94720, USA

⁷ Centre for Astrophysics, University of Southern Queensland, Toowoomba, QLD, Australia

⁸ Department of Physics & Astronomy, University of California Los Angeles, Los Angeles, CA 90095, USA

⁹ Department of Physics and Astronomy, University of Kansas, Lawrence, KS 66045, USA

Received 2024 May 18; revised 2024 July 21; accepted 2024 August 14; published 2024 October 7

Abstract

We report the observation of the transiting planet TOI-942c, a Neptunian planet orbiting a young K-type star approximately 50 Myr years old. Using the Keck/High Resolution Echelle Spectrometer, we observed a partial transit of the planet and detected an associated radial velocity anomaly. By modeling the Rossiter–McLaughlin effect, we derived a sky-projected obliquity of $|\lambda| = 24_{-14}^{+14}$ degrees, indicating TOI-942c is in a prograde and likely aligned orbit. Upon incorporation of the star's inclination and the planet's orbital inclination, we determined a true obliquity for TOI-942c of $\psi < 43^\circ$ at 84% confidence, while dynamic analysis strongly suggests TOI-942c is aligned with stellar spin and coplanar with the inner planet. Furthermore, TOI-942c is also a suitable target for studying atmospheric loss of young Neptunian planets that are likely still contracting from the heat of formation. We observed a blueshifted excess absorption in the H α line at 6564.7 Å, potentially indicating atmospheric loss due to photoevaporation. However, due to the lack of preingress data, additional observations are needed to confirm this measurement.

Unified Astronomy Thesaurus concepts: Exoplanets (498); Exoplanet systems (484); Exoplanet dynamics (490); Planetary system formation (1257); Mini Neptunes (1063)

1. Introduction

Stellar obliquity, a probe to planet-migration history, is the angle between the rotation axis of the host star and the normal of the orbital plane of the planet. The sky-projected stellar obliquity λ can be measured by the Rossiter–McLaughlin (RM) effect (D. B. McLaughlin 1924; R. A. Rossiter 1924), which reveals the distortion of stellar spectral lines during the transits due to the partial occultation of the rotating stellar surface. This phenomenon can manifest as a pattern of anomalous radial velocity (RV) variation or line shape variation during a planetary transit (e.g., Y. Ohta et al. 2005; D. C. Fabrycky & J. N. Winn 2009). The true obliquity ψ can subsequently be estimated by combining stellar inclination on the plane of the sky and the orbital inclination of the planet.

A low stellar obliquity may suggest a smooth planet-migration history in the disk, while spin–orbit misalignment is typically interpreted as indicative of a dynamically hot formation or evolutionary history. Theories on dynamically hot planet-migration span various timescales and mechanisms, including primordial disk misalignment ($\lesssim 3$ Myr; e.g., D. Lai et al. 2011; K. Batygin 2012), nodal precession (a few Myr; e.g., S. W. Yee et al. 2018), Kozai–Lidov mechanism (10^4 – 10^8 yr; e.g., D. Fabrycky & S. Tremaine 2007), and

secular chaos between planets (10^7 – 10^8 yr; e.g., Y. Wu & Y. Lithwick 2011). These mechanisms offer differing predictions regarding obliquity. Notably, these orbit-tilting excitations can occur during the early stages of planetary systems, within a few hundred Myr. Therefore, a collection of obliquity measurements from young systems can help distinguish between these mechanisms.

In addition, the existence of a planetary atmosphere can serve as another probe for investigating planet formation and migration. Planetary atmosphere loss can lead to the reductions in planetary radius and mass (e.g., S. Dong et al. 2018), which may result from atmospheric photoevaporation, happening in the system's first few Myr due to X-ray/ultraviolet irradiation from the young star (e.g., J. E. Owen & Y. Wu 2017; J. E. Owen & D. Lai 2018; S. Ginzburg et al. 2018).

TOI-942 is a young K-type star (53_{-21}^{+22} Myr; C. P. Wirth et al. 2021) hosting a pair of transiting hot Neptunes on 4 and 10 days orbits (G. Zhou et al. 2021; I. Carleo et al. 2021) discovered by the Transiting Exoplanet Survey Satellite (TESS; G. R. Ricker et al. 2014). The two planets both have radii larger than $4 R_{\oplus}$ and their host star has a projected rotational velocity $v \sin i_*$ of $\sim 15 \text{ km s}^{-1}$. With these properties, TOI-942 offers an opportunity for measuring the stellar obliquity for both Neptunian planets in a young system and constraining the mutual inclination in 3D, as well as studying atmosphere of young Neptunian planets.

The rest of the letter is organized as follows. In Section 2, we describe our spectroscopic observation of TOI-942c with Keck/High Resolution Echelle Spectrometer (HIRES). In Section 3, we describe our constraints on stellar parameters of the host star. In Section 4, we explain our joint analysis of

¹⁰ NSF Graduate Research Fellow.

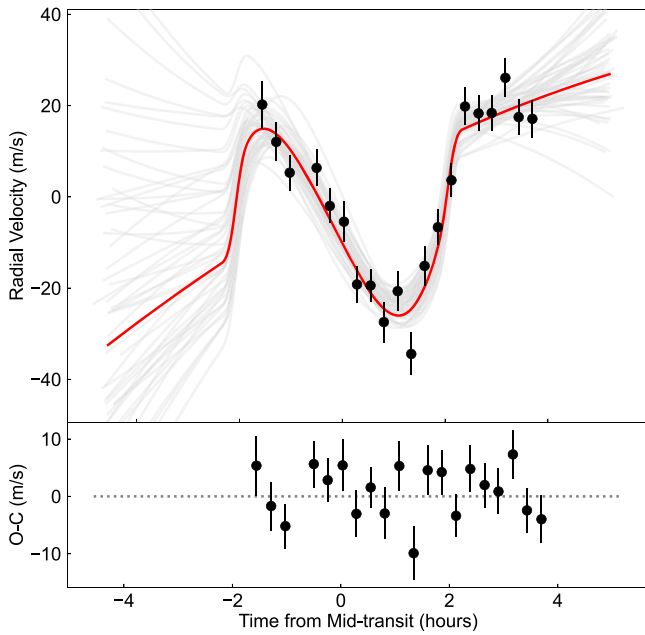


Figure 1. The radial velocities (RVs) during the transit event of TOI-942c on 2021 November 25th (UTC), measured by Keck/HIRES spectra. In the upper subplot, the solid red line is the best-fit model ($i_* = 24^{+14}_-14^\circ$), incorporating the Rossiter–McLaughlin effect and RV long-term trend. The solid gray lines are the solutions randomly selected from the Markov chain Monte Carlo sampling. In the lower panel, the residuals are given by subtracting the best-fit model.

RM effect with TESS light curve and present the stellar obliquity results. Finally, in Section 5, we discuss our results and implications from this work.

2. Spectroscopic Observations

We observed the RM effect of TOI-942c during the transit event on 2021 November 25th (UTC) with HIRES (S. S. Vogt et al. 1994) on the 10 m Keck I Telescope at Maunakea. The spectrograph has a resolution of $\sim 60,000$ and covers a wavelength range of 3643–7990 Å. An iodine cell was equipped in the optical path to the spectrograph, which provides numerous iodine absorption lines in the range of 5000–6000 Å as a reference for precise RV measurements. The spectrograph also enables tracing of the $H\alpha$ line profile variation at 6564 Å.

Our observations were scheduled based on the ephemeris from G. Zhou et al. (2021). However, due to the underestimation of transit duration, our observation started about 0.7 hr after the planet’s ingress and ended ~ 1.5 hr after the egress and did not encompass the entire transit. We set an exposure time of 900 s and reached a signal-to-noise ratio (S/N) of ~ 80 –100 near 5500 Å. In total, we obtained 21 usable spectra with 15 of them during the transit event. Another high S/N and iodine-free spectrum was obtained separately and used to generate the template spectrum to extract RV values from iodine superimposed spectra. Details of RV extraction with forward-modeling Doppler code can be found in A. W. Howard et al. (2010), and the RV data shown in Figure 1 is listed in the Appendix.

3. Stellar Parameters

We used iodine-free stellar spectrum obtained from Keck/HIRES and employed the SpecMatch-Syn pipeline¹¹ (E. A. Petigura et al. 2017) to determine the spectroscopic

parameters of TOI-942, including stellar effective temperature T_{eff} , surface gravity $\log g$, metallicity $[\text{Fe}/\text{H}]$, as well as the projected rotational velocity $v \sin i_*$. To summarize the methodology, the pipeline models the observed spectra with a synthetic model spectra, by an integration over a pre-computed grid (P. Coelho et al. 2005) within the discrete parameter space established on $(T_{\text{eff}}, \log g, [\text{Fe}/\text{H}], v \sin i_*)$.

We further estimated stellar parameters following the procedure as described in B. J. Fulton & E. A. Petigura (2018) with the Isoclassify package (D. Huber et al. 2017). In principle, we first applied the Stefan–Boltzmann law to derive the radius of the star from posterior probability distributions with inputs including stellar effective temperature, the parallax measurement from Gaia (Gaia Collaboration et al. 2021), and the K -band magnitude (which is less affected by extinction). Then we determined various stellar parameters (e.g., stellar mass) from posterior distribution by integrating over the the MESA Isochrones & Stellar Tracks (J. Choi et al. 2016) with spectroscopic parameters and the parallax and their priors.

Consequently, we obtained $R_* = 0.84 \pm 0.04 R_\odot$ for the stellar radius and $M_* = 0.86 \pm 0.03 M_\odot$ for the stellar mass. These results agree well with $R_* = 0.893^{+0.071}_{-0.053} R_\odot$ and $M_* = 0.880 \pm 0.040 M_\odot$ from I. Carleo et al. (2021), and $R_* = 0.894^{+0.056}_{-0.052} R_\odot$ and $M_* = 0.8220^{+0.0079}_{-0.0064} M_\odot$ from C. P. Wirth et al. (2021), mostly within $\sim 1\sigma$. Notably, we emphasize the difference in projected rotational velocity, although our result of $15.0 \pm 1.0 \text{ km s}^{-1}$ agrees well with $14.26 \pm 0.50 \text{ km s}^{-1}$ from C. P. Wirth et al. (2021) and $13.8 \pm 0.5 \text{ km s}^{-1}$ from I. Carleo et al. (2021) within $\sim 1\sigma$. In addition, projected rotational velocity can be estimated from rotational period and stellar radius. Using the stellar radius derived in this work and rotational period of 3.40 ± 0.37 days from G. Zhou et al. (2021), we obtained a maximum velocity of $12.5 \pm 2.0 \text{ km s}^{-1}$. This is consistent with the three spectroscopic results within $\sim 1\sigma$, but suggesting that the spectroscopic results are slightly over-estimated and the stellar inclination i_* should be close to 90° . We then calculated stellar inclination using Bayesian method described in K. Masuda & J. N. Winn (2020), and obtained a maximum posterior at 89.9° regardless of which spectroscopic rotational velocity value was used. Importantly, the projected rotational velocity is a key parameter and can be constrained by RM effect modeling. Different priors from spectroscopic measurements produce variations in obliquity constraints. Key stellar parameters are listed in Table 1.

4. Joint Light Curve and RM Analysis

TOI-942 was observed by TESS during its Sector 5 (30 minute cadence) and 32 (2 minute cadence). We obtained its light curve from the Mikulski Archive for Space Telescopes website¹² and detrended the stellar variation. To determine the sky-projected obliquity, we performed a combined analysis of the in-transit light curve and the RM effect. Prior to modeling, the TESS light curves were segmented into individual transit events to facilitate the analysis process.

For light curve modeling, we adopted the Batman package (L. Kreidberg 2015). We used a quadratic law for limb-darkening effect, and the coefficients ($u_{1,\text{TESS}}, u_{2,\text{TESS}}$), were fixed to the results which were used in C. P. Wirth et al. (2021). Since the previous three study on this system showed likely

¹¹ <https://github.com/petigura/specmatch-syn>

¹² <https://archive.stsci.edu>

Table 1
Stellar Parameters of TOI-942

Parameters (Unit)	Value and Uncertainty	References
TIC ID	146520535	A
R.A.	05:06:35.91	A
Decl.	-20:14:44.21	A
V (mag)	11.982 ± 0.026	A
K (mag)	9.639 ± 0.023	A
T_{eff} (K)	5097 ± 100	B
$\log g$ (dex)	4.47 ± 0.10	B
[Fe/H] (dex)	0.17 ± 0.06	B
$v \sin i_*$ (km s ⁻¹)	15.0 ± 1.0	B ^a
$v \sin i_*$ (km s ⁻¹)	14.26 ± 0.50	C ^a
$v \sin i_*$ (km s ⁻¹)	13.8 ± 0.5	D ^a
R_* (R_{\odot})	0.84 ± 0.04	B
M_* (M_{\odot})	0.86 ± 0.03	B
P_{rot} (days)	3.40 ± 0.37	E
P_{rot} (days)	3.39 ± 0.01	D
Age (Myr)	50^{+30}_{-20}	E
Age (Myr)	53^{+22}_{-21}	C

Notes. A: TICv8; B: This work; C: C. P. Wirth et al. (2021); D:I. Carleo et al. (2021) E: G. Zhou et al. (2021).

^a These three $v \sin i_*$ results are derived from spectroscopy.

eccentric orbit for planet c ($e < 0.8$ with 3σ upper limit for G. Zhou et al. 2021, $e = 0.175^{+0.139}_{-0.103}$ for I. Carleo et al. 2021, and $e = 0.326^{+0.23}_{-0.16}$ for C. P. Wirth et al. 2021), the eccentricity was at first set to be non-zero and fitted with the longitude of periastron using the parameter set $\sqrt{e} \cos \omega$ and $\sqrt{e} \sin \omega$. Other parameters for light curve modeling were set to be free parameters, including the logarithm of stellar density $\ln \rho_*$, the orbital period P_{orb} , the planet/star radius ratio R_p/R_* , the time of conjunction t_0 and cosine of orbital inclination $\cos i_{\text{orb}}$ with uniform priors. The boundary of $\cos i_{\text{orb}}$ was initially set between -1 and 1 , and its value was then converted to the impact factor b .

When modeling the RM effect, we followed the methodology described by T. Hirano et al. (2011), which takes into account stellar rotation, macroturbulence, thermal broadening, pressure broadening, and instrumental broadening. The macroturbulence was calculated from the scaling relation given in J. A. Valenti & D. A. Fischer (2005), thermal broadening and instrumental broadening were determined according to the formulation in T. Hirano et al. (2011), and the pressure broadening was empirically set to be 1 km s^{-1} for a K0 star (T. Hirano et al. 2011). For the limb-darkening effect, we also used a quadratic law with the coefficients ($u_{1,\text{RM}}$, $u_{2,\text{RM}}$) derived by EXOFAST¹³ with input stellar parameters (T_{eff} , [Fe/H], $\log g$) obtained from Section 3. The free parameters includes sky-projected obliquity (λ) and projected rotational velocity $v \sin i_*$. To improve sampling efficiency, they are transformed to ($\sqrt{v \sin i_*} \cos \lambda$ and $\sqrt{v \sin i_*} \sin \lambda$). In addition, RV offset γ , linear RV trend $\dot{\gamma}$, and quadratic RV trend $\ddot{\gamma}$ were set to model the intra-night RV drift caused by stellar activity and planets' orbital motion. An extra jitter term in logarithm $\ln \sigma_{\text{jit}}$ is also included to account for any kinds of additional noise. Uniform priors are set to these parameters.

We sampled the combined likelihood of the RM and transit model with a Markov chain Monte Carlo (MCMC) algorithm,

implemented in the emcee (D. Foreman-Mackey et al. 2013) code. We generated 64 random walkers, and their initials' positions were perturbed best-fit models with fixed $\sigma_{\text{jit}} = 0$. The best fits were calculated by Levenberg–Marquardt method implemented in lmfit (M. Newville et al. 2014).

We first generated several test runs, specifically with a non-zero uniform prior on eccentricity and a uniform prior on $v \sin i_*$. Consequently and by eye, we found that the maximum posterior of $|\lambda|$ was approximately 30° . We also noticed that $\sqrt{e} \cos \omega$ and $\sqrt{e} \sin \omega$ were poorly constrained and the maximum posterior of e (converted) was at 0 with $e < 0.24$ at 84%. Therefore, we defined the planet transiting in the $\cos i_{\text{orb}} > 0$ side and set $e = 0$ by fixing $\sqrt{e} \cos \omega$ and $\sqrt{e} \sin \omega$ to zero, and generated long chains with narrower uniform priors to derive the final result. These new uniform priors are listed in Table 2.

To obtain the result, we stopped the chain once it passed the Gelman–Rubin test ($\text{GR} < 1.03$). Consequently, we obtained a sky-projected obliquity of $|\lambda| = 33^{+17}_{-20}$ from the posterior, favoring a prograde and likely aligned orbit for TOI-942c. We also obtained a projected stellar rotational velocity of $v \sin i_* = 16.69^{+2.72}_{-2.40} \text{ km s}^{-1}$, roughly consistent with the spectroscopic result $15.0 \pm 1.0 \text{ km s}^{-1}$ within 1σ level. However, it is worth noting that the RM derived $v \sin i_*$ was larger than any one from spectroscopy (Table 2). This suggested an overestimate on the stellar rotation, and so did the correlating parameter sky-projected obliquity in the fitting. The overestimate on $v \sin i_*$ and $|\lambda|$ might be caused by the partial coverage of the transit. Therefore, in order to avoid the overestimate on stellar rotation, we generated MCMC chains with Gaussian priors on $v \sin i_*$. We tested two Gaussian priors following the spectroscopic results. One is $\mathcal{N}[15.0, 1.0]$ based on this work, and another one is $\mathcal{N}[14.26, 0.50]$, a same prior as in C. P. Wirth et al. (2021). As a result, we obtained $|\lambda| = 25^{+15}_{-20}$ using the our spectroscopic results as prior and $|\lambda| = 24^{+14}_{-14}$ from C. P. Wirth et al. (2021)'s prior. Free parameters and derived parameters with their uncertainties can be found in Table 2. By comparing different constraints, it is clear that with proper prior to the $v \sin i_*$, the overestimate on $|\lambda|$ was reduced to some extent.

5. Discussion

5.1. True Obliquity

TOI-942 possesses a well-determined stellar rotation period of $P_{\text{rot}} = 3.40 \pm 0.37$ days (G. Zhou et al. 2021) or $P_{\text{rot}} = 3.39 \pm 0.01$ days (I. Carleo et al. 2021). We adopt a tighter-constrained result of $P_{\text{rot}} = 3.39 \pm 0.01$ days. By combining this rotation period with the projected rotational velocity $v \sin i_*$, we can derive the posterior probability distribution for the true obliquity employing the methodology outlined in K. Masuda & J. N. Winn (2020). According to the equation proposed by D. C. Fabrycky & J. N. Winn (2009), the true obliquity ψ can be expressed as:

$$\cos \psi = \cos i_{\text{orb}} \cos i_* + \sin i_{\text{orb}} \sin i_* \cos \lambda, \quad (1)$$

where i_* is the stellar inclination, i_{orb} is the orbital inclination, and λ is the sky-projected obliquity. Given that Model 3 in Table 2 provides the best constraint on the sky-projected obliquity with $|\lambda| = 24^{+14}_{-14}$, we utilized this result along with $v \sin i_* = 14.26 \text{ km s}^{-1}$ (C. P. Wirth et al. 2021) to derive the true obliquity. Here we include a conservative uncertainty of

¹³ <https://astrutils.astronomy.ohio-state.edu/exofast/limbdark.shtml>

Table 2
Stellar and Transit Parameters of TOI-942c

Parameters (Unit)	Values and Uncertainties			Priors
	Model 1	Model 2	Model 3	
$v \sin i_*$ Prior (km s ⁻¹)	None	$\mathcal{N}[15.0, 1.0]$	$\mathcal{N}[14.26, 0.50]$	
$\ln \rho$ (ρ_\odot)	$-0.53^{+0.26}_{-0.29}$	$-0.43^{+0.19}_{-0.26}$	$-0.45^{+0.18}_{-0.26}$	$\mathcal{U}[-1, 2]$
P_{orb} (days)	$10.15609^{+0.00011}_{-0.00015}$	$10.15605^{+0.00012}_{-0.00013}$	$10.15607^{+0.00012}_{-0.00012}$	$\mathcal{U}[10.1555, 10.1565]$
t_0 (BJD-2457000)	$1447.0708^{+0.0112}_{-0.0088}$	$1447.0736^{+0.0101}_{-0.0093}$	$1447.0725^{+0.0090}_{-0.0088}$	$\mathcal{U}[1447.04, 1447.12]$
R_p/R_*	$0.0530^{+0.0014}_{-0.0012}$	$0.0528^{+0.0013}_{-0.0011}$	$0.0528^{+0.0013}_{-0.0011}$	$\mathcal{U}[0.02, 0.08]$
$\cos i_{\text{orb}}$	$0.027^{+0.012}_{-0.016}$	$0.023^{+0.012}_{-0.014}$	$0.024^{+0.013}_{-0.011}$	$\mathcal{U}[0, 1]$
$\sqrt{v \sin i_*} \cos \lambda$	$3.28^{+0.45}_{-0.65}$	$3.49^{+0.30}_{-0.52}$	$3.45^{+0.27}_{-0.48}$	$\mathcal{U}[-10, 10]$
$\sqrt{v \sin i_*} \sin \lambda$	$-2.21^{+1.35}_{-1.02}$	$-1.66^{+1.32}_{-0.87}$	$-1.56^{+0.91}_{-0.79}$	$\mathcal{U}[-10, 10]$
γ (m s ⁻¹)	$-1.89^{+16.61}_{-14.18}$	$-9.85^{+13.70}_{-10.40}$	$-8.77^{+11.71}_{-8.74}$	$\mathcal{U}[-1000, 1000]$
$\dot{\gamma}$ (m s ⁻¹ day ⁻¹)	$167.7^{+116.5}_{-140.9}$	$205.59^{+98.18}_{-132.07}$	$170.19^{+101.77}_{-121.64}$	$\mathcal{U}[-1000, 1000]$
$\ddot{\gamma}$ (m s ⁻¹ day ⁻²)	$-324.0^{+518.4}_{-413.9}$	$-294.815^{+419.60}_{-326.17}$	$-154.79^{+400.28}_{-362.68}$	$\mathcal{U}[-1000, 1000]$
$\ln \sigma$ (m s ⁻¹)	$0.86^{+0.50}_{-0.56}$	$0.88^{+0.51}_{-0.57}$	$0.91^{+0.49}_{-0.57}$	$\mathcal{U}[0, \ln(30)]$
$u_{1,\text{TESS}}$	0.4006	0.4006	0.4006	Fixed
$u_{2,\text{TESS}}$	0.2243	0.2243	0.2243	Fixed
$u_{1,\text{RM}}$	0.6436	0.6436	0.6436	Fixed
$u_{2,\text{RM}}$	0.1311	0.1311	0.1311	Fixed
$ \lambda $ (°)	33^{+17}_{-20}	25^{+15}_{-20}	24^{+14}_{-14}	Derived
$v \sin i_*$ (km s ⁻¹)	$16.69^{+2.72}_{-2.40}$	$15.21^{+0.88}_{-0.88}$	$14.36^{+0.49}_{-0.48}$	Derived ^a
ρ (ρ_\odot)	$0.59^{+0.18}_{-0.15}$	$0.65^{+0.13}_{-0.15}$	$0.64^{+0.14}_{-0.13}$	Derived ^a
R_p (R_\oplus)	$4.87^{+0.26}_{-0.26}$	$4.84^{+0.26}_{-0.25}$	$4.85^{+0.26}_{-0.25}$	Derived
T_{14} (hrs)	$4.69^{+0.48}_{-0.39}$	$4.54^{+0.43}_{-0.27}$	$4.57^{+0.41}_{-0.27}$	Derived
b	$0.45^{+0.14}_{-0.24}$	$0.39^{+0.16}_{-0.22}$	$0.40^{+0.15}_{-0.18}$	Derived
i_{orb} (°)	$88.43^{+0.91}_{-0.69}$	$88.70^{+0.78}_{-0.71}$	$88.63^{+0.66}_{-0.66}$	Derived
a/R_*	$16.5^{+1.5}_{-1.5}$	$17.1^{+1.1}_{-1.5}$	$17.0^{+1.1}_{-1.4}$	Derived
σ (m s ⁻¹)	$2.37^{+1.53}_{-1.02}$	$2.41^{+1.61}_{-1.05}$	$2.50^{+1.59}_{-1.08}$	Derived

Notes. Models 1, 2, and 3 use a fixed eccentricity of $e = 0$ and share the same priors, as determined from initial MCMC runs, except for $v \sin i_*$.

^a These two parameters are derived from RM effect.

2 km s⁻¹ on $v \sin i_*$, especially considering that macroturbulence is not well known.¹⁴ Consequently, we obtained $\psi = 30^\circ$ for maximum posterior and $\psi < 43^\circ$ at 84% confidence for a positive $\cos i_{\text{orb}}$ case, indicating a prograde orbit. Additionally, we conducted another test using the sky-projected obliquity from Model 2 in Table 2 and $v \sin i_* = 15.0$ km s⁻¹ (from our HIRES spectroscopy) with a conservative uncertainty of 2 km s⁻¹. This test yielded $\psi < 46^\circ$ at 84% confidence.

However, the physical context must be carefully considered when discussing the true obliquity of TOI-942c. First, both TOI-942b and c transit the star with observed orbital inclinations close to 90°, suggesting that planets b and c are likely coplanar with a small mutual inclination¹⁵ of $\Delta i_{\text{orb}} = 0^\circ$.

We also know that planets b and c are not in mean-motion resonance, meaning the two planets are not coupled. In such a case, a mutual inclination up to twice the true obliquity could be induced because the rapidly rotating star's oblateness can generate a quadrupole moment and torque the orbit of each planet (C. Spalding & K. Batygin 2016). If the true obliquity is as large as the estimated $\sim 30^\circ$, the mutual inclination excited by the quadrupole moment from oblateness could vary in a sinusoidal

pattern, with a maximum of twice the obliquity, i.e., $\sim 60^\circ$. Given that TOI-942b orbits in a well-aligned manner (C. P. Wirth et al. 2021) and has a small observed mutual inclination with planet c, it is more likely that planet c is also aligned and coplanar with planet b.

Further, we roughly estimated the rate of nodal precession assuming the large obliquity for TOI-942c. The precession rate can be expressed as:

$$\frac{d\Omega}{dt} = \frac{\partial \mathcal{H}}{\partial H} \quad (2)$$

where Ω is ascending node, \mathcal{H} is the Hamiltonian of planetary orbital evolution, and H is defined as $H = \cos i$, where i is planetary inclination. The Hamiltonian \mathcal{H} includes two types of interactions: the quadrupole interaction generated by stellar oblateness and the secular interaction between planets. We assumed circular orbit for simplicity and utilized the Equation (3) in C. Spalding & K. Batygin (2016) in our calculation:

$$\mathcal{H} = \underbrace{\frac{Gmm'}{a'}[(s^2 + s'^2)f_3 + ss'f_{14} \cos(\Omega - \Omega')]}_{\text{Planet-planet: Secular interaction}} - \underbrace{\frac{3GmM_*}{a} J_2 \left(\frac{R_*}{a}\right)^2 s^2 - \frac{3Gm'M_*}{a'} J_2 \left(\frac{R_*}{a'}\right)^2 s'^2}_{\text{Planet-star: quadrupole interaction}}, \quad (3)$$

¹⁴ Notably, C. P. Wirth et al. (2021) derived macroturbulence with a relatively strong Gaussian prior of 4.1 ± 0.5 km s⁻¹.

¹⁵ The mutual inclination $\Delta i_{\text{orb}} = |i_{\text{orb},1} - i_{\text{orb},2}|$ calculated from transit modeling provides a lower limit.

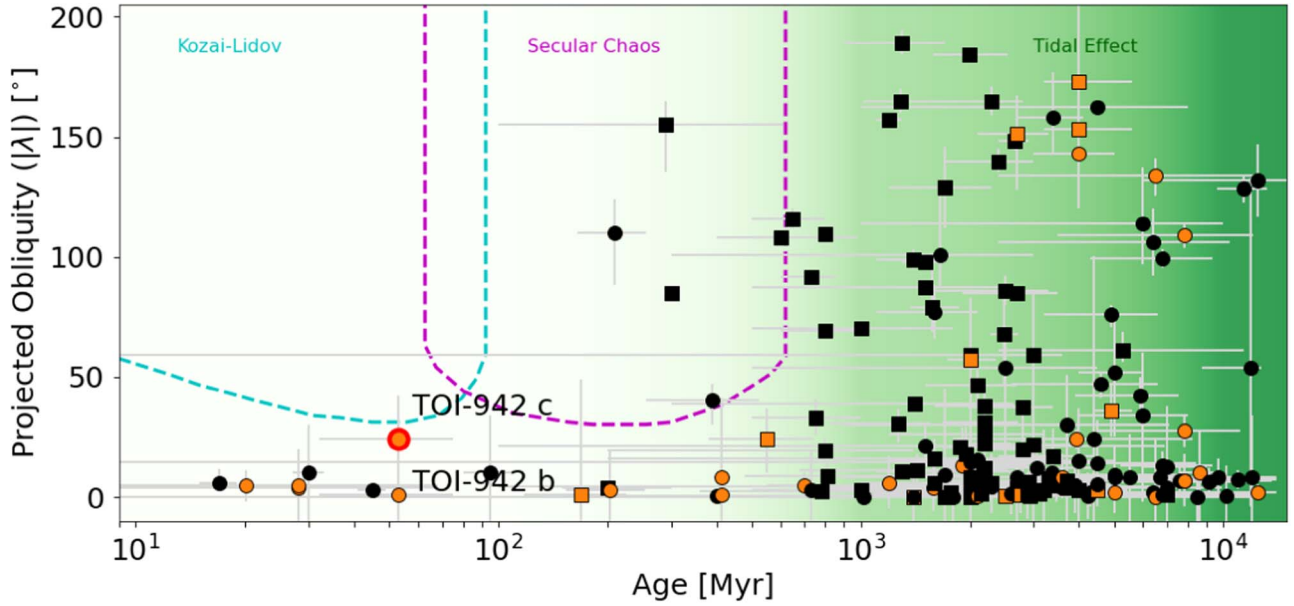


Figure 2. The absolute values of projected stellar obliquity $|\lambda|$ against host star age. Planets in single-planet systems are marked in black while those in multiplanet systems are marked in red. Host stars having effective temperature lower and higher than 6100 K (Kraft break; R. P. Kraft 1967) are, respectively, marked by circles and squares. More specifically, TOI-942c is highlighted by red edge. Different obliquity-exciting mechanisms on different timescales are marked by dashed lines in different colors, e.g., Kozai–Lidov mechanism, with a timescale shorter than a hundred Myr, and secular interaction, with a timescale in the magnitude of hundred Myr. Tidal realignment, which operates after a few hundred Myr, is shaded green with darker color indicating a stronger effect.

where the prime superscript is to distinguish two planets in the system. In the Hamiltonian, s is defined as $\sin(i/2)$, and factors f_3 and f_{14} are:

$$f_3 = -\frac{1}{2}f_{14} = -\frac{1}{2}\left(\frac{a}{a'}\right)b_{3/2}^{(1)}\left(\frac{a}{a'}\right), \quad (4)$$

where $b_{3/2}^{(1)}(\alpha)$ is the Laplace coefficient:

$$b_{3/2}^{(1)}(\alpha) \equiv \frac{1}{\pi} \int_0^{2\pi} \left[\frac{\cos \psi}{(1 + \alpha^2 - 2\alpha \cos \psi)^{3/2}} \right] d\psi. \quad (5)$$

For other factors, G is the gravitational constant, m is the planetary mass, M_* is the stellar mass, a is the semimajor axis, R_* is the stellar radius, and J_2 is the stellar oblateness. The estimate of J_2 can be found in Section 3.1 of C. Spalding & K. Batygin (2016). It is also worth mentioning that, in a two-planet system, both planets are expected to have an equal precession rate due to secular interaction (e.g., N. Bailey & D. Fabrycky 2020).

For TOI-942, we simply assumed both planets have mass of $10 M_{\oplus}$ (arbitrarily assumed), planet b is initially well aligned (C. P. Wirth et al. 2021), and planet c has a true obliquity of 30° . That is to say, we set an initial mutual inclination of $\Delta i_{\text{orb}} = 30^\circ$ regardless of its formation scenario. We estimated an oblateness of $J_2 = 7.7 \times 10^{-5}$ according to the C. Spalding & K. Batygin (2016). We separately calculated the the nodal precession rate induced by oblateness and secular interactions for TOI-942. Consequently, we estimated the nodal precession rate to be at a magnitude of $\sim 0.01 \text{ yr}^{-1}$ due to oblateness and $\sim 1^\circ \text{ yr}^{-1}$ due to secular interactions for both planets. Notably, such a precession can result in hour-long transit duration variation within 2 yr for TOI-942. However, TESS data did not show any transit duration variation for both TOI-942b and c, strongly disfavoring the high-obliquity assumption for TOI-942c.

In general, if two planets in a compact system both transit the host star, their mutual inclination must be small to ensure that

their orbits consistently intersect the stellar surface from the observer’s viewpoint. Otherwise, due to the high nodal precession rate, transit duration variations would be detected, and double transit would be inconsistent. For TOI-942 system, the largest mutual inclination can be theoretically $\Delta i_{\text{orb,max}} = i_{b,\text{max}} + i_{c,\text{max}} \approx R_*/a_b + R_*/a_c = 8^\circ$ to maintain consistent transit for both planets. Given the mutual inclination can be doubled from the quadrupole moment generated by the stellar oblateness, the maximum true obliquity of both planets in the TOI-942 system should theoretically not exceed 4° . To sum up, the dynamic analysis strongly contradicts the best-fit obliquity obtained from RM modeling and, it instead favors a well-aligned and coplanar scenario, which is about 2.3σ biased from the best-fit. This suggests that the sky-projected and true stellar obliquity result of TOI-942c should be overestimated probably owing to the incomplete coverage of the transit event.

5.2. Obliquity in Time

Figure 2 displays all the planets having the projected stellar obliquity and stellar age estimates.¹⁶ As more stellar obliquities of young planetary systems have been measured, two trends between stellar obliquity and stellar age emerge: (a) systems younger than 100 Myr are predominantly well-aligned; and (b) there are no strongly misaligned multiplanet systems younger than 1 Gyr. The trend (a) supports that orbit-tilting mechanisms which only operate during the disk-hosting stage (e.g., D. Lai et al. 2011; K. Batygin 2012) is likely not the dominant channel to generate spin–orbit misalignment (F. Dai et al. 2020; M. C. Johnson et al. 2022). The trend (b) strongly indicates that planets in young multiplanet systems, like the 50 Myr old TOI-942 system, migrated inward smoothly within the disk,

¹⁶ Data acquisition from TEPcat obliquity table at <https://www.astro.keele.ac.uk/jkt/tepcat/obliquity.html> (J. Southworth 2011) and NASA Exoplanet Archive at <https://exoplanetarchive.ipac.caltech.edu/>.

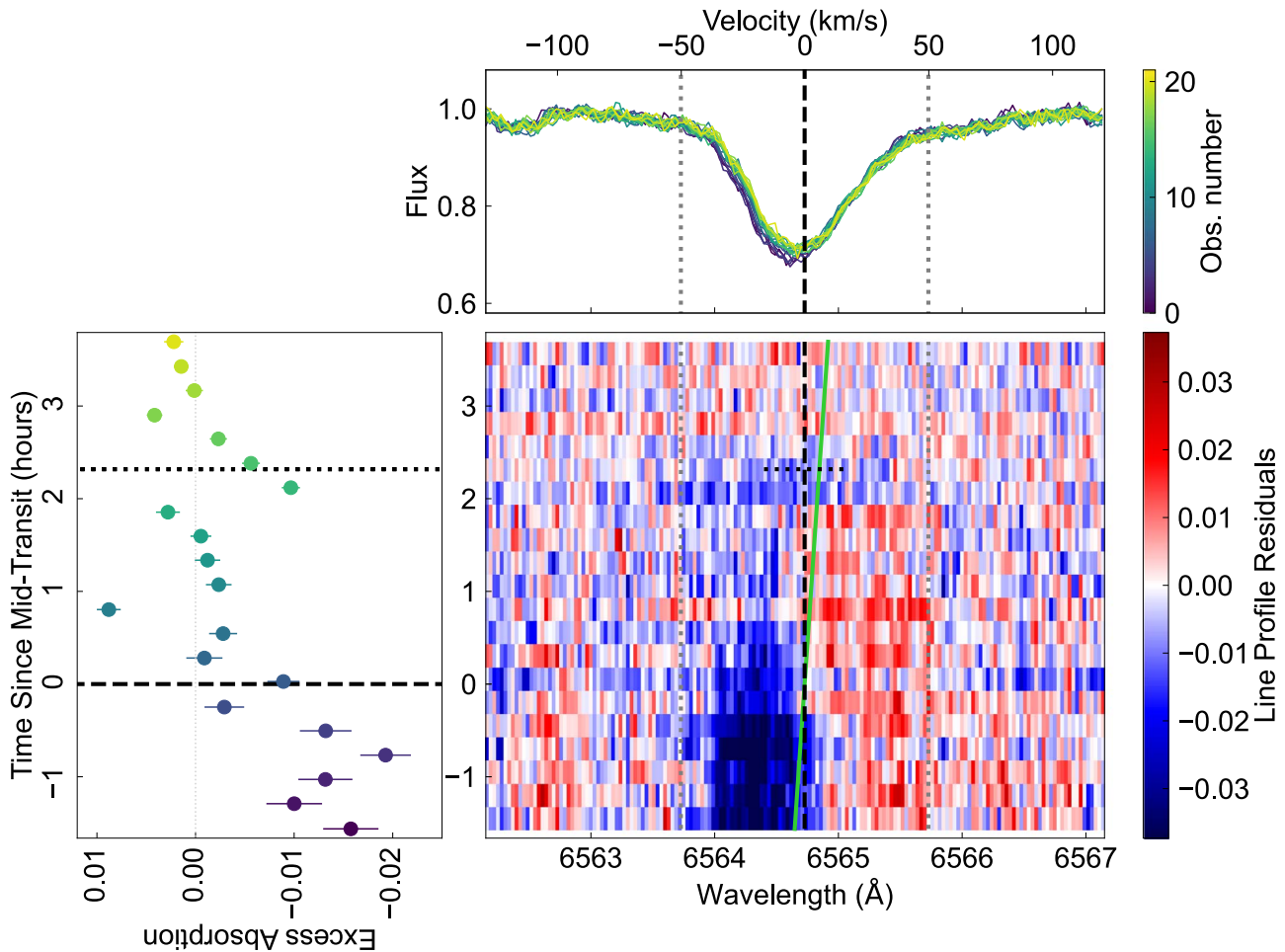


Figure 3. Top: normalized spectra of $H\alpha$ line \AA during transit event of planet c with their color indicating their observation number (epoch). The dashed line marks the line center at 6564.7 \AA , and the dotted lines indicate 1 \AA from the line center. Left: excess absorption of $H\alpha$ variation by time, with the absorption referenced by an average postegress spectrum, and calculated in a bandpass of 2 \AA centered at 6564.7 \AA . The color scale is the same for the top subplot. The dashed line and dotted line indicate midtransit and egress, respectively. Notably, ingress is not included. Main (bottom right): the measured $H\alpha$ line profile residuals as a function of time and wavelength. The dashed line and vertical dotted line correspond to the top subplot the top subplot, while the horizontal dotted line indicates the egress as in the left subplot. The predicted planetary velocity is marked by green solid line. An excess absorption and blueshift can be seen in dark blue.

underwent dynamically cool formation, and did not experience realignment prior to 1 Gyr. It is noteworthy that misalignment may occur in the early stages; for instance, K2-290 harbors two coplanar retrograde planets, believed to form through disk tilting by its close stellar companion K2-290 B (M. Hjorth et al. 2021) during the disk-hosting stage or via gravitational perturbations from its outer stellar companion K2-290 C (S. Best & C. Petrovich 2022) over a longer timescale (exceeding 100 Myr). However, due to the limited number of obliquity estimates for young multiplanet systems, none have been observed to undergo misalignment such as disk tilting. Building up a larger sample of young multiple planetary systems with stellar obliquity measurement holds the promise of constraining the origin of the misalignment.

5.3. Laboratory for Atmospheric Loss

Atmospheric loss via photoevaporation caused by high-energy radiation from the host star (J. E. Owen & Y. Wu 2017; S. Ginzburg et al. 2018) is thought to be the formation of hot Neptune desert as well as the bimodal radius distribution of sub-Neptunian planets (B. J. Fulton et al. 2017). Also,

B. J. Fulton et al. (2017) showed these small planets from Kepler are normally smaller than $3.5 R_{\oplus}$. TOI-942b and c has radii of $3.89 R_{\oplus}$ (C. P. Wirth et al. 2021) and $4.76 R_{\oplus}$, respectively, which are apparently larger than sub-Neptunes from Kepler. It suggests the TOI-942b and c may still be still contracting from the heat of formation, and as such are suitable for a comparative study because the planets are bathed in the same high-energy radiation environment except for a difference in orbital distance.

Our spectroscopic observation covers the wavelength region around 6564 \AA , enabling an examination of the $H\alpha$ line to search for excess absorption. As illustrated in Figure 3, a blueshift accompanied by a deeper absorption was observed before the midtransit and seemed to disappear after that. Three hypotheses could account for this phenomenon.

One plausible explanation is the extended planetary atmosphere. The blueshifted absorbing $H\alpha$ suggests an acceleration of the planetary atmosphere away from the star (e.g., A. D. Feinstein et al. 2021; S. Benatti et al. 2021; D. C. Linsen & A. Oklopčić 2023; D. Yan et al. 2024; J. Orell-Miquel et al. 2024). If the excess absorption starts from the ingress and continues after egress, it could signify a “comet-like” tail of the

planetary atmosphere trailing the planet, absorbing stellar photons while accelerated away by stellar winds (D. Tyler et al. 2024). Unfortunately, the absence of preingress data disabled the determination of the absorption depth prior to transit. Following up observations, covering from preingress to (at least) in-transit may address this limitation. Furthermore, if atmospheric loss is indeed the cause, we expect to observe a similar blueshifted excess absorption manifesting in the He I triplet at 10833 Å during the full transit event (e.g., M. Zhang et al. 2022; D. Tyler et al. 2024).

Two alternative hypotheses include instrumental variability and stellar activity. While slit instability in the Keck/HIRES optical path could induce spectral line fluctuations, such variation would extend across the entire spectrum rather than being confined to a specific line. Given the absence of comparable spectral variations across the entire spectrum, e.g., Na I, Ca I, Ca II, and Cr I lines (D. C. Linsen & A. Oklopčić 2023), the instrumental explanation is unlikely. Stellar activity is another scenario. Crossing spots on the stellar surface could yield similar spectral line variations (e.g., A. D. Feinstein et al. 2021; C. P. Wirth et al. 2021), yet this fails to explain the absence of concurrent variation across the entire spectrum. Since H α is a sensitive indicator for chromospheric activity, this possibility warrants careful consideration. We assessed the *S*-index of Ca II H&K lines (H. Isaacson & D. Fischer 2010) in our spectra but found no strong correlation ($r = 0.19$) between the H α excess absorption and the *S*-index. This suggests that chromospheric activity alone may not account for the observed blueshifted excess absorption.

In summary, while this study cannot confirm the true cause of the blueshifted excess absorption, atmospheric loss emerges as a promising hypothesis. Future observations hold the potential to tell us the truth.

Acknowledgments

H.Y.T. appreciates the support by the EACOA/EAO Fellowship Program under the umbrella of the East Asia Core Observatories Association. This research is supported by the National Natural Science Foundation of China (NSFC) under grant No. 12073044 and U2031144. This research has made use of the NASA Exoplanet Archive, which is operated by the California Institute of Technology, under contract with the National Aeronautics and Space Administration under the Exoplanet Exploration Program. We thank the time assignment committees of the University of California, the California Institute of Technology, NASA, and the University of Hawai'i for supporting the TESS-Keck Survey with observing time at the W. M. Keck Observatory. We gratefully acknowledge the efforts and dedication of the Keck Observatory staff for support of HIRES and remote observing. We recognize and acknowledge the cultural role and reverence that the summit of Maunakea has within the indigenous Hawaiian community. We are deeply grateful to have the opportunity to conduct observations from this mountain.

Facilities: Keck:I, TESS, Exoplanet Archive.

Software: Batman (L. Kreidberg 2015), Emcee (D. Foreman-Mackey et al. 2013), EXOFAST (J. Eastman et al. 2013), Isoclassify (D. Huber et al. 2017), lmfit (M. Newville et al. 2014), SpecMatch (E. A. Petigura 2015; S. W. Yee et al. 2017).

Appendix Additional Data and Figure

The Keck/HIRES data obtained during the transit are listed in Table 3, and the posterior distribution of Model 3 in Table 2 (i.e., the best model) is shown in Figure 4.

Table 3
Keck/HIRES Data During Transit

BJD-2457000	RV (m s ⁻¹)	σ_{RV} (m s ⁻¹)	S_{HK}	σ_{SHK}	EW _{Hα}	$\sigma_{EW_{H\alpha}}$	Airmass
2543.862651	20.22	5.20	0.736	0.001	-0.0157	0.0028	1.81
2543.873960	12.04	4.22	0.738	0.001	-0.0100	0.0028	1.69
2543.884875	5.29	3.89	0.735	0.001	-0.0132	0.0027	1.60
2543.895789	-14.18	4.01	0.736	0.001	-0.0193	0.0026	1.52
2543.906715	6.34	4.03	0.741	0.001	-0.0132	0.0026	1.46
2543.917398	-2.00	3.82	0.762	0.001	-0.0029	0.0020	1.41
2543.928891	-5.44	4.49	0.759	0.001	-0.0089	0.0016	1.38
2543.939446	-19.19	4.02	0.752	0.001	-0.0009	0.0018	1.35
2543.950430	-19.42	3.54	0.745	0.001	-0.0028	0.0014	1.32
2543.961230	-27.44	4.47	0.750	0.001	0.0088	0.0012	1.31
2543.972422	-20.67	4.35	0.741	0.001	-0.0024	0.0013	1.31
2543.983429	-34.43	4.69	0.741	0.001	-0.0012	0.0013	1.31
2543.994228	-15.14	4.32	0.730	0.001	-0.0005	0.0011	1.31
2544.005015	-6.66	3.88	0.737	0.001	0.0028	0.0012	1.33
2544.016022	3.64	3.70	0.736	0.001	-0.0097	0.0009	1.35
2544.026994	19.81	4.06	0.734	0.001	-0.0056	0.0009	1.39
2544.037966	18.29	3.87	0.741	0.001	-0.0023	0.0009	1.43
2544.048615	18.39	3.92	0.739	0.001	0.0042	0.0008	1.48
2544.059703	26.08	4.27	0.743	0.001	0.0001	0.0009	1.55
2544.070513	17.48	3.84	0.739	0.001	0.0014	0.0007	1.63
2544.081624	17.10	4.10	0.735	0.001	0.0022	0.0010	1.73

Note. The raw echelle spectra are accessible from Keck data archive (<https://koa.ipac.caltech.edu/cgi-bin/KOA/nph-KOALogin>). The weather condition at Maunakea during the observation was good, with mostly clear sky, an average humidity of 10% both inside and outside the dome, and an average seeing of approximately 0.''8, ranging between 0.''4 and 1.''6. More information about the observing weather condition can be found at <http://mkwc.ifa.hawaii.edu/>.

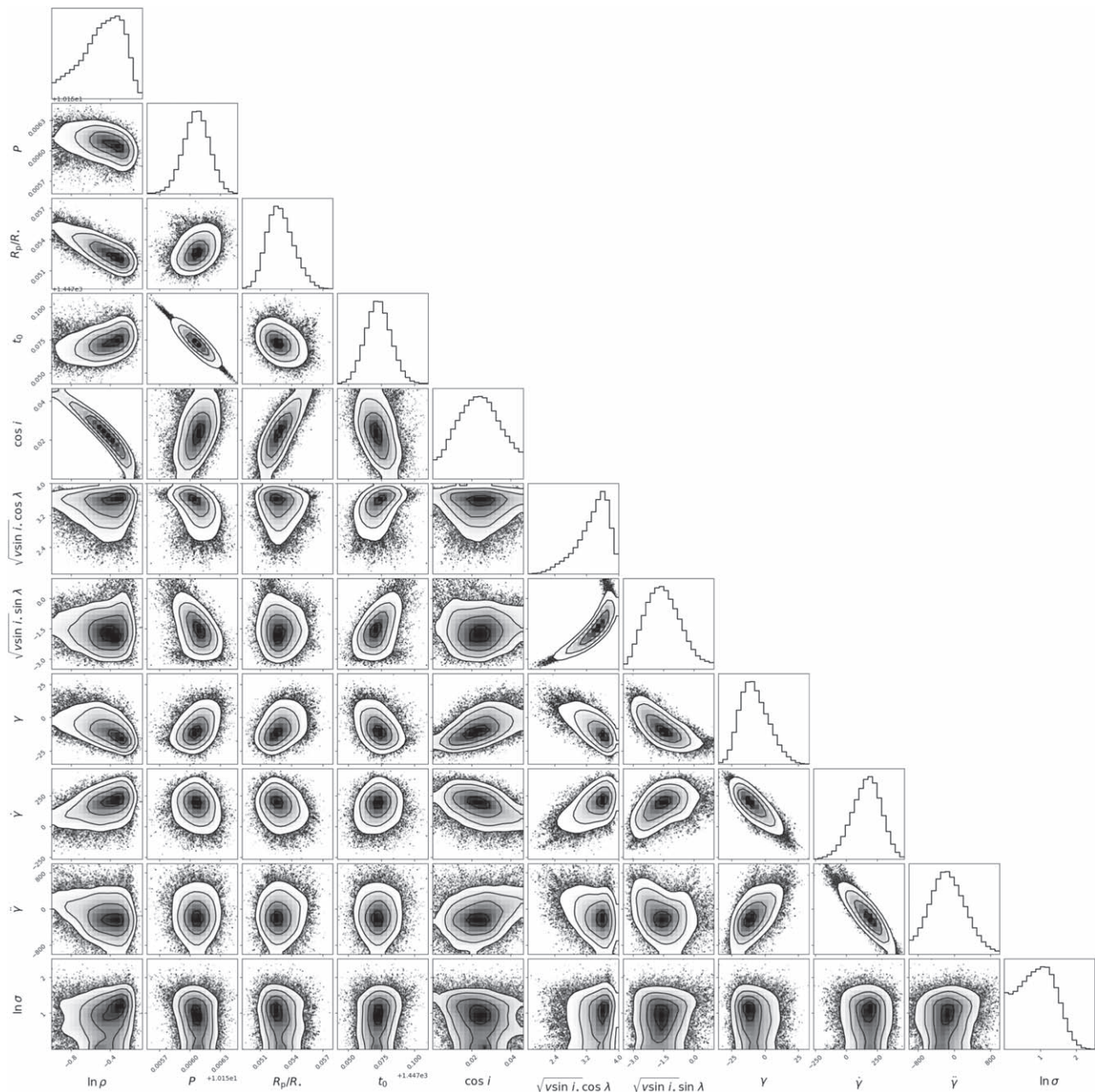


Figure 4. The posterior distribution obtained from the MCMC chain of Model 3 in Table 2 (i.e., the best model).

ORCID iDs

Huan-Yu Teng (滕环宇)  <https://orcid.org/0000-0003-3860-6297>
 Fei Dai (戴飞)  <https://orcid.org/0000-0002-8958-0683>
 Andrew W. Howard  <https://orcid.org/0000-0001-8638-0320>
 Howard Isaacson  <https://orcid.org/0000-0002-0531-1073>
 Ryan A. Rubenzahl  <https://orcid.org/0000-0003-3856-3143>
 Isabel Angelo  <https://orcid.org/0000-0002-9751-2664>
 Alex S. Polanski  <https://orcid.org/0000-0001-7047-8681>

References

- Bailey, N., & Fabrycky, D. 2020, *AJ*, 159, 217
 Batygin, K. 2012, *Natur*, 491, 418
 Benatti, S., Damasso, M., Borsa, F., et al. 2021, *A&A*, 650, A66
 Best, S., & Petrovich, C. 2022, *ApJL*, 925, L5
 Carleo, I., Desidera, S., Nardiello, D., et al. 2021, *A&A*, 645, A71
 Choi, J., Dotter, A., Conroy, C., et al. 2016, *ApJ*, 823, 102
 Coelho, P., Barbuy, B., Meléndez, J., Schiavon, R. P., & Castilho, B. V. 2005, *A&A*, 443, 735
 Dai, F., Roy, A., Fulton, B., et al. 2020, *AJ*, 160, 193
 Dong, S., Xie, J.-W., Zhou, J.-L., Zheng, Z., & Luo, A. 2018, *PNAS*, 115, 266
 Eastman, J., Gaudi, B. S., & Agol, E. 2013, *PASP*, 125, 83
 Fabrycky, D., & Tremaine, S. 2007, *ApJ*, 669, 1298
 Fabrycky, D. C., & Winn, J. N. 2009, *ApJ*, 696, 1230
 Feinstein, A. D., Montet, B. T., Johnson, M. C., et al. 2021, *AJ*, 162, 213
 Foreman-Mackey, D., Hogg, D. W., Lang, D., & Goodman, J. 2013, *PASP*, 125, 306
 Fulton, B. J., & Petigura, E. A. 2018, *AJ*, 156, 264
 Fulton, B. J., Petigura, E. A., Howard, A. W., et al. 2017, *AJ*, 154, 109
 Gaia Collaboration, Brown, A. G. A., Vallenari, A., et al. 2021, *A&A*, 649, A1
 Ginzburg, S., Schlichting, H. E., & Sari, R. 2018, *MNRAS*, 476, 759
 Hirano, T., Suto, Y., Winn, J. N., et al. 2011, *ApJ*, 742, 69
 Hjorth, M., Albrecht, S., Hirano, T., et al. 2021, *PNAS*, 118, e2017418118
 Howard, A. W., Johnson, J. A., Marcy, G. W., et al. 2010, *ApJ*, 721, 1467

- Huber, D., Zinn, J., Bojsen-Hansen, M., et al. 2017, *ApJ*, 844, 102
- Isaacson, H., & Fischer, D. 2010, *ApJ*, 725, 875
- Johnson, M. C., David, T. J., Petigura, E. A., et al. 2022, *AJ*, 163, 247
- Kraft, R. P. 1967, *ApJ*, 150, 551
- Kreidberg, L. 2015, *PASP*, 127, 1161
- Lai, D., Foucart, F., & Lin, D. N. C. 2011, *MNRAS*, 412, 2790
- Linszen, D. C., & Oklopčić, A. 2023, *A&A*, 675, A193
- Masuda, K., & Winn, J. N. 2020, *AJ*, 159, 81
- McLaughlin, D. B. 1924, *ApJ*, 60, 22
- Newville, M., Stensitzki, T., Allen, D. B., & Ingargiola, A. 2014, *LMFIT: Non-linear Least-square Minimization and Curve-fitting for Python, v0.8.0*, Zenodo, doi:10.5281/zenodo.11813
- Ohta, Y., Taruya, A., & Suto, Y. 2005, *ApJ*, 622, 1118
- Orell-Miquel, J., Murgas, F., Pallé, E., et al. 2024, *A&A*, 689, A179
- Owen, J. E., & Lai, D. 2018, *MNRAS*, 479, 5012
- Owen, J. E., & Wu, Y. 2017, *ApJ*, 847, 29
- Petigura, E. A. 2015, PhD thesis, University of California, Berkeley
- Petigura, E. A., Howard, A. W., Marcy, G. W., et al. 2017, *AJ*, 154, 107
- Ricker, G. R., Winn, J. N., Vanderspek, R., et al. 2014, *Proc. SPIE*, 9143, 914320
- Rossiter, R. A. 1924, *ApJ*, 60, 15
- Southworth, J. 2011, *MNRAS*, 417, 2166
- Spalding, C., & Batygin, K. 2016, *ApJ*, 830, 5
- Tyler, D., Petigura, E. A., Oklopčić, A., & David, T. J. 2024, *ApJ*, 960, 123
- Valenti, J. A., & Fischer, D. A. 2005, *ApJS*, 159, 141
- Vogt, S. S., Allen, S. L., Bigelow, B. C., et al. 1994, *Proc. SPIE*, 2198, 362
- Wirth, C. P., Zhou, G., Quinn, S. N., et al. 2021, *ApJL*, 917, L34
- Wu, Y., & Lithwick, Y. 2011, *ApJ*, 735, 109
- Yan, D., Guo, J., Seon, K.-i., et al. 2024, *A&A*, 686, A208
- Yee, S. W., Petigura, E. A., & von Braun, K. 2017, *ApJ*, 836, 77
- Yee, S. W., Petigura, E. A., Fulton, B. J., et al. 2018, *AJ*, 155, 255
- Zhang, M., Knutson, H. A., Wang, L., Dai, F., & Barragán, O. 2022, *AJ*, 163, 67
- Zhou, G., Quinn, S. N., Irwin, J., et al. 2021, *AJ*, 161, 2